Pacific Graphics 2015
N. J. Mitra, J. Stam, and K. Xu
(Guest Editors)

Volume 34 (2015), Number 7

The definitive version is available at http://diglib.eg.org/ and http://onlinelibrary.wiley.com/.

Geometrically Exact Simulation of Inextensible Ribbon

Zhongwei Shen, Jin Huang†, Wei Chen, Hujun Bao†

State Key Lab of CAD&CG, Zhejiang University, China

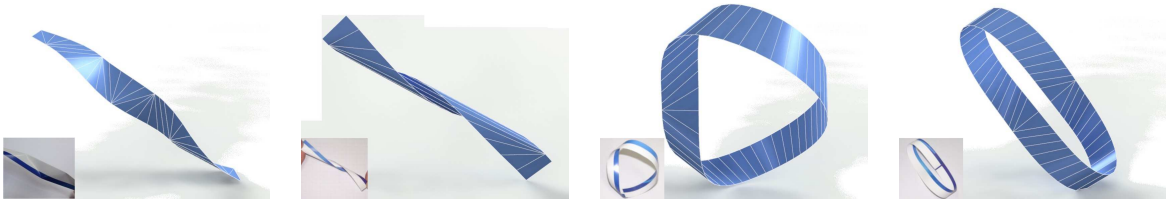

Figure 1: *Result validation with a ribbon-like paper model. From left to right: (a) twisting an initial straight and flat ribbon with stretch yields helically stacked and nearly-flat triangular facets; (b) it starts to coil if it is loosed and fastened; (c) connecting two ending points with a twisted angle π, a Mobius strip is formed; (d) changing the twisted angle to 2π yields a zero shaped loop. The simulation results in blue faithfully reproduces real-world experiments in white and blue strip.*

Abstract

Narrow, inextensible, and naturally flat ribbons have some special and interesting phenomena under isometric deformations. Although a ribbon has a shape between rod and shell, directly applying the geometric representation designed for them imposes a challenge to faithfully reproduce interesting behaviors. We thus parameterize the ribbon surface as a developable ruled surface along its centerline and represent it using a framed centerline curve. Then the elastic and kinetic energy of the ribbon surface can be equivalently yet compactly described by the framed centerline curve only. To avoid numerical singularity when developability is violated, a finite Taylor series approximation to the potential energy is adopted. Under the observation that the off-centerline part of ribbon contributes little dynamic effect, the kinetic energy is simplified with respect to the centerline velocity only. For efficiency, each time step is separated into two stages: dynamically evolving the centerline, and then quasi-statically updating the ruling. We validate the method with qualitative analysis and ribbon specific phenomena comparisons with real-world scenarios. A set of comparisons to rod and shell model is also provided to demonstrate the advantages of our method.

Categories and Subject Descriptors (according to ACM CCS):
Computer Graphics [I.3.5]: Computational Geometry and Object Modeling—Physically based modeling; Computer Graphics [I.3.7]: Three-Dimensional Graphics and Realism—Animation;

1. Introduction

An intermediate form between rod and shell that has a low ratio of width to height and negligible thickness, is called ribbon or strip. Examples of ribbon-like objects in our daily life are ornamental ribbons, film circuit boards, paper strips, and tailoring measures. Other microscopic forms include graphene sheets, crystalline ribbons, DNA, and biopolymers. The shape of a narrow, inextensible, and naturally flat ribbon is a smooth developable surface (except the rims), and thus a ruled surface. Such a special geometry property makes the ribbon exhibit some important static (Fig. 1) and dynamic (Fig. 7) behaviors that are quite challenging for existing simulation methods.

Although there are many physically based simulation approaches for rod and shell, they are not suitable for ribbons

† Corresponding authors:{hj,bao}@cad.zju.edu.cn

concerning the geometric accuracy, physical accuracy and efficiency. An accurate and efficient reproduction of the ribbon simulation remains a challenging problem. A straightforward solution would be adopting shell simulation methods and enforcing inextensibility as hard constraints. For a visually pleasing simulation, such schemes demand high mesh resolution, and large number of length constraints and thus lead to low performance. To derive an accurate and efficient model, we leverage ribbon's geometry and energy properties with the following contributions:

Geometric description We base our ribbon model on a geometrically exact and efficient curve-based representation. Compared with the methods used in the shell model, our method only requires small number of the DOFs, and the inextensible property is almost addressed in the geometrical representation, thus the cost of constraint handling in dynamic simulation is alleviated. Besides, the representation is able to handle the singularities and non-regular centerline, which are inevitable in a dynamic simulation.

Energy model Non-admissible configuration caused by the user input, contacts and numerical method will lead to infinite potential energy density and consequently the problem of singularity and instability. By using a finite Taylor series and a set of constraints to approximate the potential energy, we eliminate this problem without losing the interesting properties.

Integration method Regarding the low inertia motion as quasi-static, we propose an efficient two-stage time integration scheme: dynamically evolving the centerline according to motion equation, and then updating the ruling by optimization. Such a two-stage scheme greatly alleviates the numerical difficulties.

For validation, we study the geometric properties, static equilibrium and dynamic behavior of the simulation results through a series of comparisons with quantitative data found in mechanics literature and real-world experiments. To demonstrate the advantages of our ribbon model, we also provide a set of comparisons to the traditional rod and shell models.

2. Related Work

This section briefly reviews the most related techniques about inextensible ribbon-like objects simulation.

Rod model The most prominent reduced model for rod simulation is based on Cosserat rod theory [CCBC09] or Kirchhoff-Love rod theory [Dil92], which presents a continuum physical model for the geometrically exact simulation of rod-like objects. The model is first introduced to the graphics community in [Pai02] for virtual interaction of surgical wires. Later many works focus on different geometric representations. Representative methods include the piecewise super helical [BAC*06, Ber09], the spline-quaternion representation [TGAB08], and the piecewise linear curve with a quanternionic frame [GS07, ST07, ST08a]. A more recent work [BWR*08] employed a simplified curve-angle representation based on the parallel transport and holonomy.

To support anisotropic bend response around centerlines, two orthogonal bending directions are separated [ST07, ST08a, BWR*08], yielding a symmetric positive definite matrix for expressing the bend energy. Although the bending behavior of ribbon can be approximated with the rod model by setting the bend response in one principal direction to extreme, the essential geometric property of ribbon, developability, can not be preserved. One example is that the twisting of a ribbon-like object under tension makes its two rims elongated.

Shell model The Kirchhoff-Love shell theory [Cia00] establishes a mechanical foundation for characterizing the dynamics of thin shells or plates. Under the assumption that a shell is thin, a deformation model that considers the bend (flexural) and stretch (membrane) energies while neglecting shear is yielded. To derive a discrete bend energy, a finite element method (FEM) [BS08] or a subdivision scheme [COS00, GKS02] is applied to its mid-surface to measure the discrete curvature and length.

Based on shell theory, pioneering works for discrete bend model have been proposed [GHDS03, BMF03], in which a non-quadratic bending energy is used. Later a new quadratic bend energy with a constant Hessian [WBH*07] is derived under the assumption of isometric deformation, and a cubic energy [GGWZ07] by taking non-flat cases into consideration. For other approaches that generate physically accurate bend deformation, please refer to [HB00, CK05].

Enforce inextensibility Traditional numerical methods that enforce inextensibility constraints are the penalty method or Lagrangian method [NW99]. The most popular method is the *fast projection* method [GHF*07], which handles inextensible constraints by inaccurately solving the Lagrangian function with the range space method [NW99]. With *conforming elements* [BS08], [GHF*07] achieved 'quasi-inextensible' cloth simulation by using non-stiff springs on non-warp-weft edge. Although 'locking' is circumvented, perceptible shear is introduced, thus it can not be regarded as totally inextensible. An improvement is using *nonconforming elements* [EB08]. However, nonconforming elements introduce length error when being converted to conforming elements and incur the ghost force when enforcing conformity of boundary vertices, and such effect is amplified in the ribbon context as the transverse resolution is low and the boundary elements take a large proportion. Enforcing nonlinear inextensibility constraints is slow compared with shell bend force evaluation, because its number is proportional to the size of underlying two-dimensional surface.

Rectifying developable Rectifying developable is a kind of ruled surface, formed by the envelope of rectifying

planes of a regular curve [PM02]. It has been used for paper [BW07] and architectural modeling [PHD*10], as well as the analysis of curvature and torsion distribution of Mobius centerline [SvdH07]. Solomon et al. [SVWG12] proposed to model a developable surface by multiple developable patches from user prescribed polygonal structure. Ribbons have simpler such patch structure, but it changes in the simulation, and our method is able to automatically captures the singularities in the structure that must be manually specified in [SVWG12]. A recent work [GM10] employed a rectifying developable to study the statistical mechanics of ribbon-like polymer, but can only be used for a rough-scale shape analysis of ribbon with a regular centerline curve.

3. The Ribbon Model

In previous works [BW07, SvdH07], the geometry of a ribbon is described by a classic rectifying developable surface. The classic rectifying developable is a surface constructed from a regular curve (a curve with no curvature vanishing points). Upon the curve there exists a unique developable ruled surface formed by the envelope of its rectifying planes. In the following paragraphs, we first review the classic rectifying developable and demonstrate that it does not fit into simulation context well. Then, we propose our ribbon representation: the generalized rectifying developable.

Notation For clarity, in the following text, we will not write out the parametric variables for a quantity if no ambiguity arises. For instance, κ denotes $\kappa(u)$, S denotes $S(u,v)$. The prime symbol ' ′ ' denotes the derivative with respect to the centerline parametric value u, namely, ∇_u. Likewise, the dot symbol ' $\cdot$ ' stands for the derivative with respect to the time, i.e., ∇_t.

3.1. Rectifying Developable

A developable ribbon surface S in a rectangular shape with length l and width w can be described by its regular centerline curve $\mathbf{r}$:

$$\begin{gathered} S(u,v) = \mathbf{r}(u) + v\omega(u)\ , \\ \omega(u) = \mathbf{d}_2(u) + \eta(u)\,\mathbf{d}_3(u)\,, \\ \eta(u) = \tau(u)/\kappa(u) \\ u \in [0,l], v \in [-\omega/2, \omega/2]. \end{gathered} \tag{1}$$

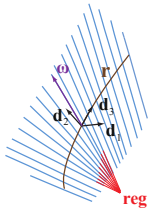

Here, S is the rectifying developable, ω is the *ruling*, and $\mathbf{M} = (\mathbf{d}_1, \mathbf{d}_2, \mathbf{d}_3) \in \mathbb{R}^{3\times3}$, $\mathbf{d}_k \in \mathbb{R}^3$ constitutes the material frame along $\mathbf{r}$, which always coincides with the Frenet frame because $\mathbf{r}$ is a geodesic on S. $\mathbf{d}_3, \mathbf{d}_1$ and $\mathbf{d}_2$ are the unit tangent, unit normal and unit binormal respectively, with centerline curvature $\kappa = \mathbf{d}'_3 \cdot \mathbf{d}_1$ and torsion $\tau = \mathbf{d}'_1 \cdot \mathbf{d}_2$. Such a frame naturally satisfies the *zero-binormal-curvature constraint*: $\mathbf{d}'_2 \cdot \mathbf{d}_3 = 0$, which is an intrinsic property of an inextensible ribbon. However, it needs a *length constraint* $c_l = \|\mathbf{r}'\| = 1$ to ensure centerline is inextensible. *No-ruling-intersection constraint* is also required to keep the *curve of regression* $\mathbf{reg}(u)$ (a curve formed by the intersection points of rulings) out of S,

$$c_{\eta'}:\ |\eta'| < 2/w. \tag{2}$$

It can be derived in a geometric way similar to [BW07], and is necessary for an admissible shape. To ensure that all the points on the ribbon are covered by rulings intersected with the centerline ($u \in [0,l]$), two ending edges of the ribbon are assumed to be parallel to $\mathbf{d}_2$, i.e. $\eta(0) = \eta(l) = 0$.

3.2. Elastic energy

The elastic energy of a naturally flat ribbon surface that undergoes isometric deformations is $\frac{1}{2}D\int H^2 dA$ [WBH*07], where D denotes the material stiffness, and H is the mean curvature with two principal curvatures κ_1, κ_2. Note zero Gaussian curvature of a developable surface transforms elastic energy into $\frac{1}{2}D\int \kappa_1^2 dA$. By differential geometry [PM02], the maximum principle curvature κ_1 along the ruling is $\kappa_1 = \frac{\kappa(1+\eta^2)}{(1+v\eta')}$, and the infinitesimal area δA in the differential form is $dA = (1+v\eta')\,dvdu$. Integrating along the transverse direction v yields the elastic energy for S:

$$V = \frac{1}{2}D\int \frac{\kappa^2\left(1+\eta^2\right)^2}{\eta'} \ln\left(\frac{1+\frac{w}{2}\eta'}{1-\frac{w}{2}\eta'}\right) du, \tag{3}$$

which has the same formulation as the one presented in [SvdH07, GM10]. The term of ln reveals the physical nature of the no-ruling-intersection constraint, i.e. an infinite energy density.

3.2.1. Truncate Infinity Energy

Computing the energy in Equation (3) is numerically problematic because the logarithm term is singular or not defined when the curve of regression is inside S. This is due to S is assumed to be developable (no-ruling-intersection constraint is hold) when deriving (3), and a 'Log Barrier' is formed in the energy to 'penalize' the curve of regression out of S. The no-ruling-intersection constraint can be removed from Equation (3) by applying the Taylor expansion to the logarithm term because the convergence condition for Taylor series is exactly the no-ruling-intersection constraint. With some standard derivations, we have:

$$V = \sum_{a=0}^{\infty} \frac{w^{2a+1}D}{2^{2a+1}(2a+1)} \int (\eta')^{2a}\left(\kappa^2 + 2\tau^2 + \tau^2\eta^2\right) du, \tag{4}$$

where a is the order of the Taylor expansion. V is empirically truncated at 5th-order in our experiments. By using an explicit constraint to prevent ruling-intersection in simulation, such an approximation eliminates infinity in the energy without losing much accuracy.

3.2.2. Handle Non-Regular Centerline

The ruling direction η is critical for the energy in Equation (3). If the centerline is a regular curve, we can derive a well-defined η from the Frenet frame. However, the centerline can be non-regular (i.e. in flat or wavy shape). When there is non-regular point on the centerline, the Frenet frame may flip, and leads to difficulty on evaluating η'. Such an issue is caused by the definition of curvature and normal: $\kappa = \|\mathbf{d}_3'\|$ and $\mathbf{d}_1 = \mathbf{d}_3'/\kappa$ in the Frenet frame, which keeps $\kappa \geq 0$, and $\mathbf{d}_1$ in the same direction as $\mathbf{d}_3'$. It can be addressed by rotating the Frenet frame along $\mathbf{d}_3$ with π, so that it aligns $\mathbf{d}_1$ to the normal on one side of the orientable ribbon, and then becomes a smooth and differentiable material frame. In § 6.2, we show that the non-orientable surface can also be described with this representation by introducing transition function.

In a non-regular point with $\kappa = 0$, τ must be zero, because the inextensible ribbon can not be twisted without bending. In this case, the ruling $\eta = \tau/\kappa$ is in $0/0$ indeterminate form, which means that ω is not well-defined. However, the shape and orientation of the ribbon is not affected by the choice of η in such a region.

3.3. Kinetic energy

To derive the kinetic energy we sum up the translational kinetic energy of all mass particles on S, $T = \frac{1}{2}\rho \int \mathbf{v}^2 dA$ where ρ is the mass density, $\mathbf{v} = \dot{S} = \dot{\mathbf{r}} + v\dot{\omega}$ is the translational velocity at an infinitesimal area δA. The kinetic energy can be derived from its frame-adapted centerline:

$$T = \frac{1}{2}\rho \int \left(w\dot{\mathbf{r}}^2 + \frac{w^3}{12}\dot{\omega}^2 + \frac{w^3}{6}\eta' \dot{r}\dot{\omega} \right) du. \tag{5}$$

Evaluating Equation (5) is complicated, especially after the expansion of $\dot{\omega}$. Here we simplify it by ignoring low inertial and high frequency motion in the ribbon simulation. Note that a quasi-static twist treatment for rod [BWR*08] is based on the observation that the twist wave travels much faster than the bend wave. To adopt the instant twist wave propagation scheme we need to identify the twist counterpart for the ribbon. Fortunately, the generalized rectifying developable enables an effective means to extract the twist component comparable with rod twist. By regarding the change of the ruling $\omega = \mathbf{d}_2 + \eta \mathbf{d}_3$ as twist on the ribbon (in analogy to the change of the binormal $\mathbf{d}_2$ in the Cosserat rod model), the simplified kinetic energy is:

$$T = \frac{1}{2}\rho w \int \dot{\mathbf{r}}^2 du. \tag{6}$$

3.4. Generalized coordinates

The choice of the generalized coordinates affects performance and stability. Considering the non-admissible configuration is inevitable, directly deriving the material frame from the centerline is problematic, thus we use the material frame explicitly instead of deriving it from the centerline. The ruling direction is heavily involved in geometry representation, checking admissibility and energy terms, so, the same to the material frame, we also deal it a free variable in the following generalized coordinates g, which is efficient and singularity-free:

$$g = \{\mathbf{q}, \eta, \mathbf{r}\}, \tag{7}$$

where $\mathbf{q}$ is a quaternion that represents the material frame $\mathbf{M}$, $\mathbf{r}$ and η are the same as before.

Except for the *Unit-quaternion constraint* $c_u = \|\mathbf{q}\| = 1$, which ensures a valid quaternion, these variables are under a set of constraints from rectifying developable to make g represent an admissible inextensible ribbon shape:

1. *parallel* $c_{para} = \mathbf{r}'/\|\mathbf{r}'\| - \mathbf{d}_3(\mathbf{q}) = 0$.
2. *zero-binormal-curvature*: $\mathbf{d}_2(\mathbf{q})' \cdot \mathbf{d}_3(\mathbf{q}) = 0$.
3. *length*: $c_l = \|\mathbf{r}'\| - 1 = 0$.
4. *no-ruling-intersection*: $c_{\eta'} : |\eta'| < 2/w$.
5. *same-torsion*: $c_{s\tau} = \kappa(\mathbf{q})\eta - \tau(\mathbf{q}) = 0$.

With constraints 1 and 2, $\mathbf{q}$ is related to the Frenet frame of $\mathbf{r}$. η is related to $\kappa(\mathbf{q})$ and $\tau(\mathbf{q})$. In a flat region, $\kappa = \tau = 0$, thus the constraint leaves η free.

However, the energy formula (4) serves as a heuristic for defining the ruling distribution at curvature-vanishing region. By making rulings as perpendicular to the centerline as possible, energy change of the major (the $0th$ order) component is expected to be small when a flat ribbon is perturbed. Thus, for $\kappa(u) = 0$ in $u \in [u_a, u_b]$ with the boundary condition $\kappa(u_a)$ and $\kappa(u_b)$, η is defined by,

$$\min_{\eta} \int_{u_a}^{u_b} \eta^2(u)\, du, \;\; \text{s.t. } c_{\eta'}(u), u \in [u_a, u_b]. \tag{8}$$

By using such a generalized coordinates, the configuration can temporarily run into a non-admissible configuration under the user control, collision response and intermediate numerical step. Under these constraints introduced above, the configuration will be efficiently projected back to the nearest admissible one for a valid ribbon.

External constraints Our explicit centerline and frame representation makes it convenient to apply external force and torque. Besides, the *p*osition constraint can be easily incorporated as $c_p = \mathbf{r}(u_k) - \mathbf{p}_k = 0$ where $\mathbf{p}_k$ denotes a fixed point in space, and the *orientation constraint* can be implemented by restricting the frame rotation around centerline: $c_o = \dot{\mathbf{d}}_1(\mathbf{q}) \cdot \mathbf{d}_2(\mathbf{q}) = 0$. Users can specify the orientation quaternion at the nodes, but our orientation constraint provides a more atomic constraint than this, which leaves the DOF of rotating the tangent direction and just constrains the rotating around the center line.

4. Discretization

In this section, we seek a discrete representation that converges to the corresponding smooth part via the finite element method.

4.1. Discrete quantities

We discretize the ribbon centerline $\mathbf{r}$ into n nodes $\mathbf{r}_0,...,\mathbf{r}_{n-1}$, n scalars $\eta_0,...,\eta_{n-1}$ (including two on boundaries), and $n-1$ segments $\mathbf{e}^0,...,\mathbf{e}^{n-2}$, with $\mathbf{e}^i=\mathbf{r}_{i+1}-\mathbf{r}_i$, and one quaternion on each segment: $\mathbf{q}^0,...,\mathbf{q}^{n-2}$. We use the lower indices to indicate the node quantities and the upper indices for the segment quantities. Piecewise linear shape functions are used to reconstruct $\mathbf{r}$, $\mathbf{q}$ and η:

$$(\mathbf{r}')^i=\frac{\mathbf{r}_{i+1}-\mathbf{r}_i}{\bar{l}^i},\ (\mathbf{q}')_i=\frac{2\left(\mathbf{q}^{i+1}-\mathbf{q}^i\right)}{\bar{l}^{i+1}+\bar{l}^i},\ (\eta')^i=\frac{\eta_{i+1}-\eta_i}{\bar{l}^i}, \quad (9)$$

$$\tilde{\mathbf{r}}^i=\frac{\dot{\mathbf{r}}_i+\dot{\mathbf{r}}_{i+1}}{2},\ \tilde{\mathbf{q}}_i=\frac{\bar{l}^i\mathbf{q}^i+\bar{l}^{i+1}\mathbf{q}^{i+1}}{\bar{l}^{i+1}+\bar{l}^i},\ (\tilde{\eta}')_i=\frac{\eta_{i+1}-\eta_{i-1}}{\left(\bar{l}^i+\bar{l}^{i-1}\right)}, \quad (10)$$

where the tilde symbol '~' indicates the quantities reconstructed from the shape functions, and the quantities with bar symbol '-' denote values evaluated at the resting state. For example, $\bar{l}^i=\left\|\bar{\mathbf{e}}^i\right\|$ is the length of $\mathbf{e}^i$ at the resting state. The strain rates expressed in terms of quaternion $\mathbf{q}=(q_x,q_y,q_z,q_w)^T$ in discretized fashion are, binormal bending $\gamma_i(\mathbf{q})=2\mathbf{B}_1\tilde{\mathbf{q}}_i\cdot(\mathbf{q}')_i$, curvature $\kappa_i(\mathbf{q})=2\mathbf{B}_2\tilde{\mathbf{q}}_i\cdot(\mathbf{q}')_i$ and torsion $\tau_i(\mathbf{q})=2\mathbf{B}_3\tilde{\mathbf{q}}_i\cdot(\mathbf{q}')_i$, where $\mathbf{B}_k\in\mathbb{R}^{4\times4}$ are constant skew-symmetric matrices [ST07],

$$\mathbf{B}_k\mathbf{q}=\begin{cases}(q_w,q_z,-q_y,-q_x)^T & k=1\\(-q_z,q_w,q_x,-q_y)^T & k=2\\(q_y,-q_x,q_w,-q_z)^T & k=3.\end{cases}$$

4.2. Energy discretization

The discrete elastic energy V of Equation (4) involves $n-2$ terms on nodes between the adjacent segments, with each integration over $\frac{1}{2}\left(\bar{l}^{i+1}+\bar{l}^i\right)$. The discrete kinetic energy T of Equation (6) consists of $n-1$ terms on each segment, with each integration over segment $\bar{l}^i$:

$$\begin{aligned}V&=\sum_{a=0}^{\infty}\frac{w^{2a+1}D}{2^{2a+2}(2a+1)}\sum_{i=0}^{n-3}\left(\bar{l}^i+\bar{l}^{i+1}\right)\left(\tilde{\eta}'\right)_i^{2a}E_i\\T&=\frac{1}{8}\rho w\sum_{i=0}^{n-2}\bar{l}^i\left(\dot{\mathbf{r}}_i+\dot{\mathbf{r}}_{i+1}\right)\cdot\left(\dot{\mathbf{r}}_i+\dot{\mathbf{r}}_{i+1}\right),\end{aligned} \quad (11)$$

where $E_i=\kappa_i^2(\mathbf{q})+2\tau_i^2(\mathbf{q})+\tau_i^2(\mathbf{q})\eta_i^2$.

4.3. Constraint discretization

The discretization for all non-external constraints is straightforward except for the orientation constraint which needs special care,

$$c_{l,i}=l^i\cdot l^i-\bar{l}^i\cdot\bar{l}^i=0, \quad (12)$$

$$c_{\eta',i}:\left|(\eta_{i+1}-\eta_i)/\bar{l}_i\right|<2/w, \quad (13)$$

$$c_{\gamma,i}=-2\mathbf{B}_1\tilde{\mathbf{q}}_i\cdot\left(\mathbf{q}'\right)_i=0, \quad (14)$$

$$c_{s\tau,i}=\kappa_i(\mathbf{q})\eta_i-\tau_i(\mathbf{q})=0 \quad (15)$$

$$c_{para,i}=(\mathbf{r}_{i+1}-\mathbf{r}_i)/\bar{l}_i-\mathbf{d}_3^i=0, \quad (16)$$

$$c_{u,i}=\left\|\mathbf{q}^i\right\|=1. \quad (17)$$

Frame constraint conversion By explicitly representing the frame and centerline, we can reformulate the nonlinear orientation constraint c_o into a linear frame constraint by using the time parallel transport technique [BAV*10, KJM10]. Time parallel transport transports a vector along a curve formed by the tangent manifold integrated in time. With a discrete space and time setting, parallel transport for the material frame on the ribbon centerline can be viewed as a linear transformation: $\mathbf{d}_{j,t_1}^k=P_{dis}\left(\mathbf{d}_{3,t_0}^k,\mathbf{d}_{3,t_1}^k\right)\mathbf{d}_{j,t_0}^k,\ j\in\{1,2\}$, where the subscripts t_0 and t_1 denote two consecutive time points, P_{dis} is either the minimum rotation between two vectors [BWR*08] or the corresponding two reflections [WJZL08]. Since both $\mathbf{d}_{3,t_0}^k$ and $\mathbf{d}_{3,t_1}^k$ can be calculated from the centerlines $\mathbf{r}_{t_0}$ and $\mathbf{r}_{t_1}$, we can explicitly evaluate $\mathbf{d}_{1,t_1}^k$ and $\mathbf{d}_{2,t_1}^k$, and cast the orientation constraint into a simple linear *frame constraint*:

$$c_{f,k}=\mathbf{q}^k-\mathbf{q}_{t_1,f}^k=0, \quad (18)$$

where $\mathbf{q}_{t_1,f}^k$ is the material frame converted from the material frame $\mathbf{M}_{t_1}^k$. Because a quaternion has a double covering on a rotation matrix [Han06], $\mathbf{q}_{t_1,f}^k$ is set to be closer to $\mathbf{q}^k$ on its parametric surface $\mathbf{S}^3$ via: $\mathbf{q}_{t_1,f}^k=\mathrm{sgn}\left(\mathbf{q}^k\cdot\mathbf{q}_{t_1,f}^k\right)\mathbf{q}_{t_1,f}^k$, where $\mathrm{sgn}()$ is the sign function. Note that indistinguishable 2π clockwise or counter-clockwise rotation ($\mathbf{q}^k\cdot\mathbf{q}_{t_1,f}^k=0$) rarely happens because the step size in the simulation prevents such radical changes.

5. Numerical Simulation

We present the entire procedure of our simulation (Algorithm 1) for the geometrically exact simulation of ribbon and discuss numerical methods that employed.

5.1. Two-stage time stepping

For efficiency, we focus on the low frequency motion by treating the twist motion quasi-statically. First, the centerline is evolved dynamically by integrating an ODE, which is driven by the potential energy of the ribbon relayed by parallel constraint. Then, an optimization process 'dissipates' the motion of twist under current configuration of centerline and prepares the elastic force to evolve centerline for the subsequent time step. The two steps take all the admissible constraints into account and thus lead to a valid trajectory

with dynamics. In summary, one time step consists of the two stages *opt* and *ode*:

$$\begin{aligned}(\mathbf{q}_{t_0},\eta_{t_0},\mathbf{r}_{t_0},\dot{\mathbf{r}}_{t_0}) &\xrightarrow{ode} (\mathbf{q}_{t_0},\eta_{t_0},\mathbf{r}_{t_1},\dot{\mathbf{r}}_{t_1}) \\ &\xrightarrow{opt} (\mathbf{q}_{t_1},\eta_{t_1},\mathbf{r}_{t_1},\dot{\mathbf{r}}_{t_1}).\end{aligned} \tag{19}$$

Dynamically evolving centerline In stage *ode*, the centerline is evolved by integrating the following ODE with symplectic Euler,

$$\mathbf{M}\ddot{\mathbf{r}} = -\nabla_{\mathbf{r}} E_{para} + \mathbf{F}_e, \tag{20}$$

where $\mathbf{M}$ is a diagonal matrix that represents the lumped mass distribution on the centerline node derived from the kinetic energy in Equation (6), $\mathbf{F}_e$ denotes user exerted force or gravity. The energy that transfers elastic energy from $(\mathbf{q},\eta)$ to $\mathbf{r}$ is defined as $E_{para} = w_{para}\|c_{para}\|^2$, where w_{para} denotes a weight. To enforce c_l via postprocessing, we find the stationary point of Lagrangian $L_{\dot{\mathbf{r}}} = \frac{1}{2}\dot{\mathbf{r}}^T\mathbf{M}\dot{\mathbf{r}} + \lambda_l c_l$ by using fast projection [GHF*07]. After solving *ode*, damping is incorporated by isotropically dissipating the velocity as $\mathbf{r}_t \leftarrow \mu_t\mathbf{r}_t, \mathbf{r}_{nt} \leftarrow \mu_{nt}\mathbf{r}_{nt}$, where the coefficient μ_t for the tangent direction is usually set to be in 0.8-0.9, and μ_{nt} for velocity on cross section is 0.98. In this step, the center line configuration steps forward according to the current ruling configuration, which will be changed in the *opt* step.

Quasistatically update ruling In stage *opt*, we iteratively solve an optimization problem to keep the ruling configuration consistent to the updated center line configuration. Each iteration is composed of a single L-BFGS step to the unconstrained problem and a following up projection for constraints. Be more specific, in each iteration, we first apply a single step of L-BFGS to the unconstrained problem to obtain $\mathbf{q}^*, \eta^*$

$$\min_{(\mathbf{q},\eta)} V + E_{para}, \tag{21}$$

where V is the elastic energy in Equation (11). Then the internal constraints $c_{\eta'}$, c_γ and $c_{s\tau}$ are enforced by approaching stationary point of the following Lagrangian

$$\begin{aligned}L_{\mathbf{q},\eta} =& \frac{1}{2}\Delta\mathbf{q}^T\mathbf{I}\Delta\mathbf{q} + \frac{1}{2}\Delta\eta^T\mathbf{I}\Delta\eta \\ &+ \lambda_{\eta'}c_{\eta'} + \lambda_\gamma c_\gamma + \lambda_{s\tau}c_{s\tau},\end{aligned} \tag{22}$$

where $\mathbf{I}$ is the identity matrix, $\Delta\mathbf{q} = \mathbf{q} - \mathbf{q}^*$ and $\Delta\eta = \eta - \eta^*$. Each newton iteration can be solved with the range space method [NW99], which solves the first order optimal condition of Equation (22) with decoupled Newton iteration: the multipliers are solved from a linear equation first, and then updating unknown variables. We solve the linear equation for the multipliers with partial Projected-Gauss-Seidel method, by only projecting $\lambda_{\eta'} \geqslant 0$ so that no sticking arises when enforcing inequality constraint $c_{\eta'}$. We terminate the *opt* loop with the change of gradients of two consecutive iterations is less than 1% and norm of constrains (without $c_{\eta'}$) is less than 10^{-6} and $c_{\eta'} \geqslant 0$ holds. The method usually ends within 10 iterations. For the unit-quaternion constraint ($c_{u,i}$) and the frame constraint ($c_{f,k}$), we directly correct them, namely, $\mathbf{q}^i \leftarrow \mathbf{q}^i \Big/ \left\|\mathbf{q}^i\right\|$ and $\mathbf{q}^i \leftarrow \mathbf{q}^{i,f}$ are performed when $\mathbf{q}$ changes. This experimental method may not lead to the exact solution of optimizing Equation 21 under the constraints, but the results are acceptable in all our experiments.

Torsional Dynamics Compensation Although the inertia from the angular velocity is not significant for a narrow ribbon, especially for a constrained ribbon, we can still enrich the dynamics by taking it into account for handling free floating case. To augment torsional dynamical effects, instead of using $\mathbf{q}_0$ as the initial value for optimization of Equation (21), we mimic effect of rotational inertia by accumulating $\mathbf{q}_0$ (the result of ODE step) with the angular portion along the centerline $\mathbf{q}_0 = \mathbf{q}_0 + \mathbf{d}_3(\mathbf{r}) \cdot \left(\mathbf{q}_0\mathbf{q}_{-1}^{-1}\right)$, where $\mathbf{q}_{-1}$ is the previous step of $\mathbf{q}_0$. Then Equation (21) can also be augmented with a torsional inertia guiding term $E_I(\mathbf{q}) = w_I\left\|\mathbf{d}_3(\mathbf{r}) \cdot \left(\mathbf{q}\mathbf{q}_{-1}^{-1} - \mathbf{q}_0\mathbf{q}_{-1}^{-1}\right)\right\|^2$, where w_I is a weighting that reflects the inertia tensor. We choose $w_I = \frac{\Gamma|K_D|}{I_{ir}\dim_K}, \Gamma \in [0,1]$ where I_{ir} is the torsional inertia around the centerline and Γ measures the internal torsional damping, $|K_D|$ is the l_1 norm of the diagonal part of stiffness matrix K (Hessian matrix of the elastic energy V), and $\dim_K$ is its dimension.

Accuracy of Elastic Force The choice of the weighting w_{para} influences dynamic accuracy and performance. With a large w_{para}, dynamics can be more accurate, but step size of *ode* is smaller and more efforts are required in the optimization process, and it is more likely to generate force in wrong direction due to early termination of *opt* (like the ghost force [ST08b]). In consideration of performance and dynamics, we choose $w_{para} = \alpha\frac{|K_D|}{\dim_K}$ and $\alpha \in \left[10, 10^2\right]$ (Fig. 2).

Algorithm 1 One step of our ribbon simulation algorithm

Require: ribbon configuration $(\mathbf{r}_{t_0}, \mathbf{q}_{t_0}, \eta_{t_0})$
Require: position constraint $\mathbf{p}_k$, frame constraint $\mathbf{q}_{t_0,f}$
1: dynamically update centerline motion (20) and enforce c_l
2: time-parallel transport $\mathbf{q}_{t_0,f}$ to $\mathbf{q}_{t_1,f}$ §4.3
3: **while** not converged **do**
4: quasi-static update ruling motion (21)
5: enforce $c_{\eta'}$, c_γ, $c_{s\tau}$ (22) and c_f, c_u
6: update ruling in curvature vanishing region (8)
7: **end while**
8: generate mesh from state $(\mathbf{r}, \mathbf{M}, \eta)$ for rendering §6.1

6. Results

We validate our model in three aspects: geometric property, static equilibrium and dynamic behavior. Comparisons with rod and shell are also included to demonstrate the performance and quality advantages.

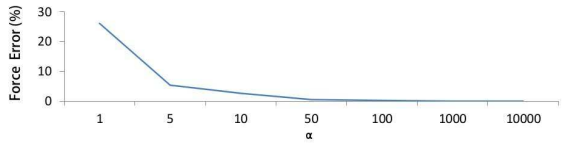

Figure 2: *Dynamics accuracy for different choice of* α.

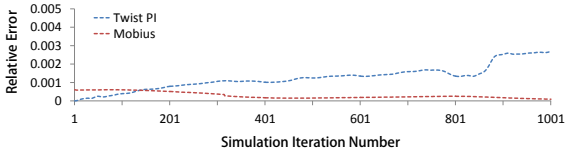

Figure 3: *The relative error statistics of the total area measured on two examples: the twist of an open ribbon with aspect ratio 10 by angle PI and a Mobius strip with an aspect ratio* $\frac{l}{w} = \frac{5}{4}\pi$.

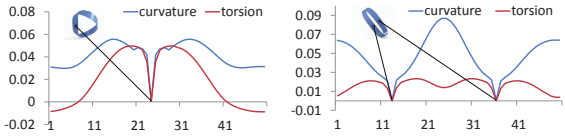

Figure 4: *The curvature and torsion distribution of a closed loop in its equilibrium shape with an aspect ratio* $\frac{l}{w} = 5\pi$. *Left: the distribution of a Mobius strip. Our result faithfully reproduces the single curvature-vanishing point on the centerline predicted in [SvdH07]. Right: in the rest* 2π *loop, our result reveals two curvature-vanishing points.*

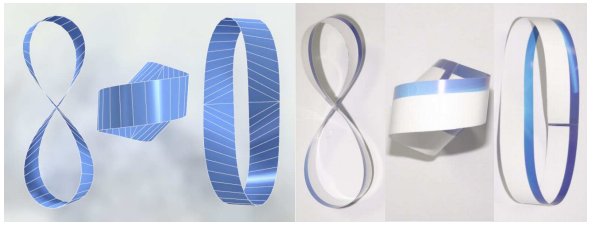

Figure 5: *Three views of the* 2π *closed ribbon loop with aspect ratio* $\frac{l}{w} = 5\pi$ *(left: our result; right: real-world one).*

6.1. Geometric properties

Reconstructing surface The shape of a ribbon surface is reconstructed from all quadrangles (or triangles on the ruling intersection area) formed by the adjacent rulings and two rims. Since the points on ruling are, $\hat{\mathbf{r}} = \mathbf{r} + v\omega$ and with $v = \pm\frac{w}{2}$, they are also on the rims. The normal of the vertex $\hat{\mathbf{r}}$ is the normal $\mathbf{d}_1$ on the centerline, because all points on the same ruling share the same normal. To increase visual smoothness, we use the cubic spline to interpolate the centerline $\mathbf{r}$ and the linear interpolation for the ruling and normal (η and $\mathbf{q}$).

Isometry test We use the total area preservation as a metric to benchmark isometric deformation. Fig. 3 shows a sequence of relative error of the total area measured for two simulation examples. By enforcing all various constraints in tolerance 10^{-6}, the relative area error is lower than 1% and inextensibility is achieved.

6.2. Static equilibrium

For validation, we study the shape of a non-orientable loop (a Mobius strip) by comparing the curvature κ and torsion τ distribution along the centerline with those obtained in mechanics literature [SvdH07] (Fig. 4), and a real-world comparison (Fig. 1), as well as three views of the 2π twisted orientable loop (Fig. 5).

Loop case We define the transition operations to extend our method to orientable and non-orientable loop cases. Suppose a closed loop is formed by concatenating an open-ended ribbon centerline $\mathbf{r}(u)$, $u \in [0, l]$ at $u = 0$ (or $u = l$) with a clockwise twist of angle φ viewed from positive parametric direction. First, a closed loop does not have boundary, so the assumption of straight ending edges $\eta(0) = \eta(l) = 0$ is no longer required. The constraint $\mathbf{r}_0 - \mathbf{r}_{n-1} = 0$ is required for a close loop of centerline. In non-orientable case, to invert $\mathbf{q}^{n-2}$ to side of $\mathbf{q}^0$, we rotate it along $\mathbf{e}^{n-2}$ with angle $-\varphi - 2\pi$. η, $\kappa(\mathbf{q})$ and $\tau(\mathbf{q})$ can be inverted to the other side by changing the sign. Based on these quantities, an additional elastic energy, a zero-binormal-curvature constraint and a no-ruling-intersection constraint at the concatenating point are added.

We further validate our approach by twisting a flat ribbon under large longitudinal tension. A buckling pattern with helically stacked nearly-flat triangular facets appears on ribbon surface, as reported in [KSvdH11] (Fig. 1). With decreasing and increasing of the load, the ribbon starts to coil into a cylindrical shape (Fig. 1). Both are verified by the real-world experiment using paper strip (Fig. 1).

6.3. Dynamic behavior

To investigate the dynamics accuracy, we compare the motion sequence of a releasing coiled belt (Fig. 7 left two) with a real-life example. Under gravity and damping, the released ribbon transfers its potential energy to kinetic energy and starts to swing before it stops. Our approach achieves quality similar to the real one (see companion video). To validate feasibility of the quasi-static ruling motion treatment, another comparison is made by releasing a twisted belt under tension (Fig. 7 right two). After releasing, the twist component of elastic energy quickly dissipates, matching with the real-world experiment (see companion video).

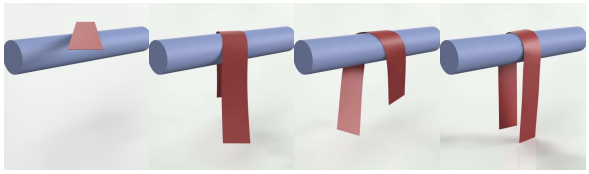

Figure 6: *A ribbon falling down from the sky and hanging on a cylinder. It swings back and forth smoothly with only 20 segments (with each element interpolated into three for rendering), demonstrating that our algorithm is able to generate visually pleasing contact motion at low resolution in a very efficient manner.*

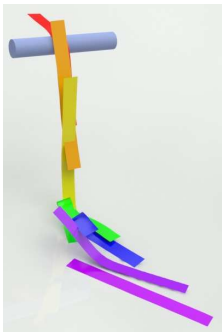

We perform collision detection on the reconstructing surface (§6.1). Contact normal and contact point $S_c(u,v)$ can be obtained. Then we augment Equation (22) into $L_{\dot{\mathbf{r}},\mathbf{q},\eta} = \frac{1}{2}\dot{\mathbf{r}}^T\mathbf{M}\dot{\mathbf{r}} + \frac{1}{2}\Delta\mathbf{q}^T\mathbf{I}\Delta\mathbf{q} + \frac{1}{2}\Delta\eta^T\mathbf{I}\Delta\eta + \lambda_n c_n + \lambda_t c_t + \lambda_{\eta'} c_{\eta'} + \lambda_\gamma c_\gamma + \lambda_{s\tau} c_{s\tau}$ and follow [OTSG09] to find the stationary point of this Lagrangian, where c_n and c_t are contact constraint and friction constraint with respect to $(\dot{\mathbf{r}},\mathbf{q},\eta)$. The wrap figure in this section shows 7 sequential frames when a stiff ribbon slides from cylinder and falls onto the ground. Fig. 6 shows a scene that a soft ribbon slides smoothly on the cylinder after falling to it.

6.4. Performance

With the new energy model built upon the centerline, the computational complexity is linearly proportional to the number of centerline nodes, namely, $O(n)$. The performance is influenced by the order of the Taylor expansion a. In our experiments we choose $a = 5$ such that in most cases the elastic energy residual is less than 0.01%. In Algorithm 1, Step 4 handles the constraints including no-ruling-intersection constraint which may vary in complexity. Note that its complexity is still bounded by $O(n)$. Table 1 shows the performance for various scenarios.

6.5. Comparison with rod model

We compare the ribbon surface generated by our method and that by the rod model [BWR*08]. Under large tension, twisting a ribbon simulated by the rod model will result in two elongated rims (Fig. 8. Rod model's stiffness ratio is set as: $\alpha_1 : \alpha_2 : \beta = 10^4 : 1 : 2$, where α_1 and α_2 are bend coefficients in two orthogonal directions and β is the twist coefficient. Similar results can be expected using different stiffness ratios or different models [ST07], as the underlying Cosserat (Kirchhoff-Love) rod model allows twist without bend.

Fig.#	Seg.#	h	opt	Δt	ode	other	total
1(a)	35	0.05	7.99	20.0	1.53	1.52	11.04
1(b)	20	0.05	4.04	10.0	0.75	0.65	5.44
1(c)	50	0.03	11.21	10.0	1.88	1.20	14.29
1(d)	50	0.03	10.58	10.0	1.93	1.45	13.96
6	20	0.05	3.62	10.0	0.78	0.66	5.06
7(L)	45	0.05	8.83	20.0	1.70	1.12	11.65
7(R)	45	0.05	8.32	20.0	1.81	1.09	11.22

Table 1: *Performance in milliseconds for one iteration of Algorithm 1 on 2.66GHz Core i7 920 CPU with single thread. Notations: Figure appeared in the paper (Fig.#), segment of centerline* $\mathbf{r}$ *(Seg.#), step size of optimization(h), time cost of opt part (opt, §5), time step of time integration (Δt), time cost of ode part (ode, §5), time cost of other part in our algorithm (other) and total time (total).*

Model	m	n	Δt	t_{sol}	t_{len}	t_{bd}	total
Conf.	12	36	0.1	9.61	42.87	NA	52.48
Conf.	4	36	1.0	2.56	13.15	NA	15.71
Nonconf.	8	26	0.1	12.62	47.71	6.42	66.75
Nonconf.	4	21	1.0	3.87	12.31	4.58	20.76

Table 2: *Performance in milliseconds for one single iteration of shell simulation method using nonconforming and conforming elements on the scenario of Fig. 8. The columns from the left to the right are the number of longitudinal vertices (n), number of the transverse ones (m) in the (conforming) mesh, time step Δt (ms), time for each implicit Euler integration solve (t_{sol}), time for enforcing length constraints with fast projection (t_{len}), time for enforcing boundary constraints with fast projection (t_{bd}) and total time (total).*

6.6. Comparison with shell model

We compare our ribbon model with the shell model using nonconforming elements [EB08] and conforming elements [GHF*07]. Since [GHF*07] is only 'quasi-inextensible', we replace the non-stiff springs on non-warp-weft edge with hard constraints. The Jacobian of length constraint is split into two and enforcement is done in tandem to avoid rank deficiency in planar case. We drive both models with the same discrete bend model [WBH*07]. The length constraint and boundary constraint (using nonconforming elements) are enforced with fast projection until the length error is lower than 1%. Time integration is performed by implicit Euler integration.

Bend force evaluation of shell is very efficient. However, our goal is to simulate developable surface and the bend model is only justified under isometric deformation. Hence the enforcement of nonlinear length (developability) constraints is the bottleneck. For a (conforming) mesh with n longitudinal vertices and m transverse vertices, the number of length constraints is $3mn$ when using conforming elements and $6(m-1)(n-1)$ when using nonconforming elements. Note that there are only $4n$ developability constraints in our method involved in solving equation. To achieve the same coil result (Fig. 1), m needs to be at least 10. Moreover, according to Courant-Friedrichs-Lewy (CFL) stability criterion [PTVF07], with a more dense tessellation, the time step of shell model is over an order smaller than our method.

Figure 7: *Results of our approach faithfully capture the dynamics of belt motion. The rainbow color denotes 7 frames sampled sequentially on a simulation sequence.* ***Left Two:*** *releasing a coiled belt with frames sampled on frame 1,13,25,37,49,61,73 in simulation sequence. After releasing, the left one with high stiffness swings 'vigorously' while the right one with low stiffness quickly collapses.* ***Right Two:*** *releasing a twisted belt with frames sampled on frame 1,8,16,75,125,200,250 in simulation sequence. After releasing, the left one with high stiffness dissipates twist energy quicker than the right one with low stiffness.*

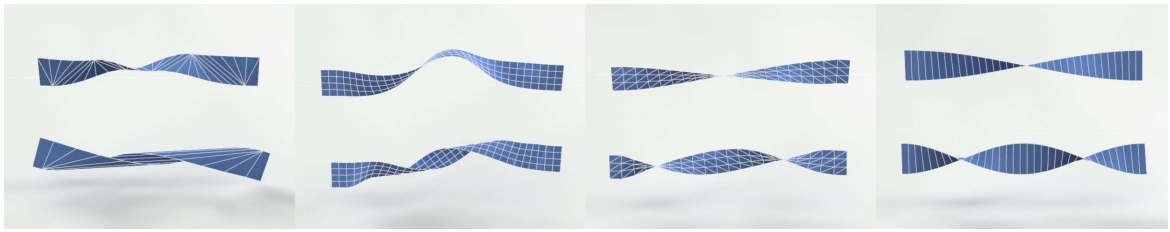

Figure 8: *Shapes of a ribbon with aspect ratio* $\frac{5}{2}\pi$ *under tension twisted by* π *and* 2π *generated by different methods under low resolution / comparable compute time. From left to right: results produced by our method with 35 segments, by shell model using conforming elements with* 4×36 *resolution, by shell model using nonconforming elements (in conforming shape) with* 4×21 *resolution and by rod model method with 35 segments. Results produced by our method shows high resemblance to real life (Fig. 1), while others fail to reproduce quality results at similar computational cost for a single step. The shell model using conforming elements has the most close shape to groundtruth but still can not reproduce the triangular buckling pattern, and can not coil as close as ribbon model due to insufficient DOF. To achieve the similar coil result, at least 10 transverse vertices are required. The shell model using nonconforming elements deviates from the groudtruth even further. The rod model simply fails to keep developable, with relative area error 1.86%* (π)*, 7.19%* (2π)

Thus our method is much more efficient than the shell methods. More detailed timing data can be found in Table 2. At the same computational cost with low resolution (when m is around 3-5), the shell fails to capture complex geometry of a twisted ribbon surface (Fig. 8).

7. Conclusion

In this paper we have endeavored to design a both geometrically accurate and efficient simulation approach tailored to developable ribbon like objects, which fills the gap between rod and shell simulation with diverse shape expressibility, efficient and singularity free numerical methods, as well as easily incorporatable external constraints.

Our approach is based on the assumption that the ribbon surface can be represented by a generalized rectifying developable. It is not true when ribbon is very soft and contains wrinkles caused by deformation. Consequently, our approach is suitable for ribbon made from leather, rubber or metal that wrinkles are not perceptible.

Despite the benefits from the usage of the quaternion in representing a material frame, it introduces three non-linear constraints and complicates the numerical simulation. The two-stage strategy in time stepping largely alleviates the numerical challenges, but introduce a heuristic parameter, the weight E_{para} of parallel penalty. Although the experimental setting works well in our results, it scarifies accuracy for robust and performance. Other efficient methods for time integration with accurate parallel constraint are very valuable future works. Using other material frame representation methods may worth a try to solve this problem. The current model of kinetic energy is simple and not accurate enough. Although the experimental torsional dynamics compensation makes the dynamics more plausible, a better kinetic energy formulation with balanced accuracy and efficiency is definitely interesting. The model proposed in the paper works

well for inextensible ribbons under zero-thickness assumption, e.g. papers or film strips. Another interesting future work is to extend the method to handle nearly inextensible ribbons and taking the thickness into account for better accuracy for leather and rubber ribbon.

Acknowledgements

This work was partially supported by NSFC (No.61170139, No.61210007), Fundamental Research Funds for the Central Universities (No. 2015FZA5018) and Major Program of National Natural Science Foundation of China (61232012). We would also like to thank the anonymous reviewers for their valuable comments and suggestions.

References

[BAC*06] BERTAILS F., AUDOLY B., CANI M.-P., QUERLEUX B., LEROY F., LÉVÊQUE J.-L.: Super-helices for predicting the dynamics of natural hair. *ACM TOG (SIGGRAPH 06) 25*, 3 (2006), 1180–1187. 2

[BAV*10] BERGOU M., AUDOLY B., VOUGA E., WARDETZKY M., GRINSPUN E.: Discrete viscous threads. *ACM TOG (SIGGRAPH 10) 29*, 4 (2010), 116:1–116:10. 5

[Ber09] BERTAILS F.: Linear time super-helices. *CGF (EG 09) 28*, 2 (2009), 417–426. 2

[BMF03] BRIDSON R., MARINO S., FEDKIW R.: Simulation of clothing with folds and wrinkles. In *SCA '03* (2003), pp. 28–36. 2

[BS08] BRENNER S. C., SCOTT L. R.: *The Mathematical Theory of Finite Element Methods*. Springer-Verlag, 2008. 2

[BW07] BO P., WANG W.: Geodesic-controlled developable surfaces for modeling paper bending. *CGF (EG 07) 26*, 3 (2007), 365–374. 3

[BWR*08] BERGOU M., WARDETZKY M., ROBINSON S., AUDOLY B., GRINSPUN E.: Discrete elastic rods. *ACM TOG (SIGGRAPH 08) 27*, 3 (2008), 63:1–63:12. 2, 4, 5, 8

[CCBC09] COSSERAT E., COSSERAT F., BROCATO M., CHATZIS K.: *Théorie des corps déformables*. A. Hermann Paris, 1909. 2

[Cia00] CIARLET P. G.: *Mathematical Elasticity: Theory of Shells*. Elsevier, 2000. 2

[CK05] CHOI K. J., KO H. S.: Research problems in clothing simulation. *CAD 37*, 6 (2005), 585–592. 2

[COS00] CIRAK F., ORTIZ M., SCHRÖDER P.: Subdivision surfaces: a new paradigm for thin-shell finite-element analysis. *Int. J. Numer. Methods Eng. 47*, 12 (2000), 2039–2072. 2

[Dil92] DILL E. H.: Kirchhoff's theory of rods. *Archive for History of Exact Sciences 44*, 1 (1992), 1–23. 2

[EB08] ENGLISH E., BRIDSON R.: Animating developable surfaces using nonconforming elements. *ACM TOG (SIGGRAPH 08) 27*, 3 (2008), 1–5. 2, 8

[GGWZ07] GARG A., GRINSPUN E., WARDETZKY M., ZORIN D.: Cubic shells. In *SCA '07* (2007), pp. 91–98. 2

[GHDS03] GRINSPUN E., HIRANI A. N., DESBRUN M., SCHRÖDER P.: Discrete shells. In *SCA '03* (2003), pp. 62–67. 2

[GHF*07] GOLDENTHAL R., HARMON D., FATTAL R., BERCOVIER M., GRINSPUN E.: Efficient simulation of inextensible cloth. *ACM TOG (SIGGRAPH 07) 26*, 3 (2007), 49. 2, 6, 8

[GKS02] GRINSPUN E., KRYSL P., SCHRÖDER P.: Charms: a simple framework for adaptive simulation. *ACM TOG (SIGGRAPH 02) 21*, 3 (2002), 281–290. 2

[GM10] GIOMI L., MAHADEVAN L.: Statistical mechanics of developable ribbons. *Phys. Rev. Lett. 104*, 23 (2010), 238104. 3

[GS07] GRÉGOIRE M., SCHÖMER E.: Interactive simulation of one-dimensional flexible parts. *CAD 39*, 8 (2007), 694–707. 2

[Han06] HANSON A. J.: *Visualizing Quaternions*. MK/Elsevier, 2006. 5

[HB00] HOUSE D., BREEN D. E.: *Cloth Modeling and Animation*. AK Peters, Ltd., 2000. 2

[KJM10] KALDOR J. M., JAMES D. L., MARSCHNER S.: Efficient yarn-based cloth with adaptive contact linearization. *ACM TOG (SIGGRAPH 10) 29*, 4 (2010), 105:1–105:10. 5

[KSvdH11] KORTE A. P., STAROSTIN E. L., VAN DER HEIJDEN G. H. M.: Triangular buckling patterns of twisted inextensible strips. *Proc. R. Soc. A 467*, 2125 (2011), 285. 7

[NW99] NOCEDAL J., WRIGHT S. J.: *Numerical Optimization*. Springer, 1999. 2, 6

[OTSG09] OTADUY M. A., TAMSTORF R., STEINEMANN D., GROSS M.: Implicit Contact Handling for Deformable Objects. *CGF (EG 09) 28*, 2 (2009), 559–568. 8

[Pai02] PAI D. K.: Strands: Interactive simulation of thin solids using cosserat models. *CGF (EG 02) 21*, 3 (2002), 347–352. 2

[PHD*10] POTTMANN H., HUANG Q., DENG B., SCHIFTNER A., KILIAN M., GUIBAS L., WALLNER J.: Geodesic patterns. *ACM TOG (SIGGRAPH 10) 29*, 4 (2010), 43:1–43:10. 3

[PM02] PATRIKALAKIS N. M., MAEKAWA T.: *Shape Interrogation for Computer Aided Design and Manufacturing*. Springer-Verlag, 2002. 3

[PTVF07] PRESS W. H., TEUKOLSKY S. A., VETTERLING W. T., FLANNERY B. P.: *Numerical Recipes 3rd Edition: The Art of Scientific Computing*. Cambridge University Press, 2007. 8

[ST07] SPILLMANN J., TESCHNER M.: CoRdE: Cosserat rod elements for the dynamic simulation of one-dimensional elastic objects. In *SCA' 07* (2007), pp. 63–72. 2, 5, 8

[ST08a] SPILLMANN J., TESCHNER M.: An adaptive contact model for the robust simulation of knots. *CGF (EG 08) 27*, 2 (2008), 497–506. 2

[ST08b] SPILLMANN J., TESCHNER M.: Cosserat nets. *IEEE TVCG 15* (2008), 325–338. 6

[SvdH07] STAROSTIN E. L., VAN DER HEIJDEN G. H. M.: The shape of a Möbius strip. *Nat. Mater. 6*, 8 (2007), 563–567. 3, 7

[SVWG12] SOLOMON J., VOUGA E., WARDETZKY M., GRINSPUN E.: Flexible developable surfaces. *CGF (SGP 12) 31*, 5 (2012), 1567–1576. 3

[TGAB08] THEETTEN A., GRISONI L., ANDRIOT C., BARSKY B.: Geometrically exact dynamic splines. *CAD 40*, 1 (2008), 35–48. 2

[WBH*07] WARDETZKY M., BERGOU M., HARMON D., ZORIN D., GRINSPUN E.: Discrete quadratic curvature energies. *CAGD 24*, 8-9 (2007), 499–518. 2, 3, 8

[WJZL08] WANG W., JUTTLER B., ZHENG D., LIU Y.: Computation of rotation minimizing frames. *ACM TOG 27*, 1 (2008), 1–18. 5